Manuscript for *Journal of Nuclear Materials* –revised-

Title: **Study on the Chemical Structure and Actinide Leaching of MCCI Debris**

Authors: Akira Kirishima[*a], Akito Nagatomo[a], Daisuke Akiyama[a], Takayuki Sasaki[b], and Nobuaki Sato[a]

Affiliation: [a]Institute of Multidisciplinary Research for Advanced Materials, Tohoku University, 1-1 Katahira, 2-chome, Aoba-ku, Sendai 980-8577, Japan

[b]Department of Nuclear Engineering, Kyoto University, Kyoto Daigaku-Katsura, Nishikyo, Kyoto 615-8530, Japan

Footnotes: [*]Corresponding author,

Contents:

Text pages	23 (excluding this page)
Tables	2
Figures	10
Supplementary materials	5
Corresponding author	Akira Kirishima
Address	Institute of Multidisciplinary Research for Advanced Materials, Tohoku University, 1-1 Katahira 2-chome, Aoba-ku, Sendai 980-8577, Japan
Tel	+81-22-217-5143
Fax	+81-22-217-5143
E-mail	kiri@tohoku.ac.jp

Abstract

To understand the chemical structure and stability of molten core-concrete interaction (MCCI) debris generated by the Fukushima Daiichi nuclear power plant accident in Japan in 2011, simulated MCCI debris consisting of the U-Zr-Ca-Si-O system and other simpler systems were synthesized and characterized. ^{237}Np and ^{241}Am tracers were doped for the leaching tests of these elements and U from the simulated debris. The MCCI debris were synthesized by heat treatment at 1200 °C or 1600 °C, in reductive (Ar + 10% H_2) or oxidative (Ar + 2% O_2) atmospheres. Subsequently, the debris were used for actinide leaching tests with water. Zr and Ca formed a solid-solution with the UO_2 matrix, such as $(Zr_yU_{1-y})O_{2+x}$, $(Ca_yU_{1-y})O_{2+x}$, and $(Ca_zZr_yU_{1-y-z})O_2$, which stabilized the matrix and suppressed actinide leaching from the simulated debris. On the other hand, the cement components (CaO and SiO_2) in the debris formed a glass-like coating on the debris, which also remarkably suppressed the leaching of actinides.

Keywords

Fukushima NPP, Severe Accident, Fuel Debris, Molten Core-Concrete Interaction, Actinides, Leaching

1. Introduction

On March 11, 2011, a loss of coolant accident (LOCA) occurred at the Fukushima Daiichi nuclear power plant (NPP) in Japan after a cold shutdown because of an undersea megathrust earthquake and a subsequent tsunami. The nuclear fuels reacted with the zircaloy (Zry) cladding, control rods, and other reactor structural materials such as stainless steel and concrete at high temperature, forming molten mixtures. As a result, a variety of chemical compounds and shapes of nuclear fuel debris were formed in the reactors under different conditions. For the safe retrieval and long-term storage of the fuel debris in the decommissioning mission of the damaged reactors, the understanding of the chemical and physical properties of the fuel debris is critically important. The debris are, however, highly radioactive and release a lot of heat, which prevents direct access and sampling of them. Therefore, acquired information on the real debris in Fukushima Daiichi NPP is so far limited to the radiation dose near the debris, the sampled small precipitates at the bottom of the primary containment vessel (PCV) in unit-1 and unit-3 and inside the PCV in unit-2, and the morphological information such as picture images of the debris using remote devices and visualized internal structure images of the PCV using cosmic ray muons [1,2,3,4]. The Tokyo Electric Power Company (TEPCO) and the International Research Institute for Nuclear Decommissioning (IRID) reported that the precipitated small particles (ca. 2 μm) at the bottom of the PCV in unit-1 consisted of a Zr-rich solid-solution phase (U, Zr)O_2, while a particle sampled inside the PCV in unit-2 had a similar composition, i.e., ($Zr_{0.64}$, $U_{0.36}$)O_2, which had a tetragonal crystal structure analyzed by electron diffraction [2]. The structure and composition of these precipitated particles in the PCV were interpreted by TEPCO and IRID to be parts of the body of the fuel debris. This is the only information obtained so far regarding

63 the chemical character of the real debris in Fukushima NPP by direct analysis, which is obviously
64 insufficient to assess the risks associated with the debris left in the damaged reactor units and predict the
65 procedures for the safe handling and storage of the debris in the future.

66 Therefore, in order to provide supportive information towards understanding the chemical properties
67 and stabilities of the fuel debris, we have initiated a basic chemical research into the nuclear fuel debris
68 by synthesizing and analyzing several types of simulated fuel debris in laboratories. In this part of the
69 study, we categorize the type of debris into slightly damaged fuels (U-O system), fuel-zircaloy (Zry)
70 cladding debris (U-Zr-O system), fuel-alloy debris (U-stainless steel-O system), and molten core-concrete
71 interaction (MCCI) debris (U-concrete component-O system). Because of the high and long-term
72 radioactive toxicity, actinide's behavior in the debris will have a significant impact on the future
73 management of the radioactive waste released by the Fukushima NPP decommissioning activities.
74 Therefore, in previous studies, we reported the crystal structures of the simulated fuel-zircaloy (Zry)
75 cladding debris (U-Zr-O system) and the leaching behavior of the actinides in it, which are very important
76 factors indicating the chemical stability of the debris [5-9]. The studies revealed that the formation of the
77 solid-solution phase $Zr_yU_{1-y}O_2$ chemically stabilizes the matrix of the debris so that the leaching of the
78 fission product (FP) nuclides and actinides to seawater and pure water are effectively suppressed by the
79 interaction between U and Zr. Further, the progress of this solid-solution formation depends on the redox
80 atmosphere and temperature during the debris generation. Additionally, we recently reported the phase
81 structure and chemical state of the fuel-alloy debris including Zr (U-Zr-stainless steel components-O
82 system) by synthesizing the simulated fuel debris [10].

Following the previous studies, the MCCI debris are investigated in this study by the same procedure, i.e., synthesis, characterization, and leaching tests of the simulated MCCI debris. Due to the penetration of the molten core from the reactor pressure vessel to the bottom of the PCV, it is expected that a certain amount of debris existed as MCCI debris in the damaged reactors of Fukushima NPP [1]. Kitagaki et al. [11] conducted a thermodynamic evaluation of the MCCI debris using the thermodynamic equilibrium calculation tools. They concluded that the solid-solution phases, (U, Zr)O_2 and (Zr, U)SiO_4, were the expected main phases of the MCCI debris in Fukushima NPP, while the formation of (Zr, U)SiO_4 phase was limited due to the reaction kinetics reason. To reliably predict the distribution of fuel debris including MCCI debris in the damaged reactors of Fukushima NPP by computer simulations, Hidaka et al. improved the MCCI computation models [12,13]. To justify the thermodynamic equilibrium calculation, computer simulations, and accident progression analysis concerning the MCCI debris, a scientific evidence obtained by a controlled laboratory experiment and analysis is highly necessary, especially in the chemical aspect of the MCCI debris. Therefore, we synthesized and analyzed the simulated MCCI debris consisting of the U-Zr-Ca-Si-O system and other simpler systems for a comparison in this study. Concrete is a mixture generally made from cement, sand, water, and other materials; on the other hand, cement is a powder consisting of CaO, SiO_2, Al_2O_3, Fe_2O_3, MgO, and other minor components. As the first step for the MCCI debris study, we chose CaO and SiO_2 as the main concrete components since they generally occupy more than 80% of the cement. These concrete components were mixed with UO_2 and ZrO_2 for the synthesis of the simulated fuel debris. The effect of other cement materials such as Al_2O_3 and Fe_2O_3 on the chemistry of the MCCI debris would be studied in our future work. To conduct the actinide leaching test with minor

103 actinides such as Np and Am, their tracers (i.e., ^{237}Np and ^{241}Am) were doped into UO_2, and then the
104 tracer-doped UO_2 was used for the synthesis of the simulated MCCI debris.
105
106 **2. Materials and methods**
107 2.1 Synthesis of the simulated MCCI debris
108 As the initial material for the simulated fuel debris, UO_2 doped with ^{237}Np and ^{241}Am tracers were
109 synthesized by the ammonium diuranate (ADU) co-precipitation procedure described in our previous
110 studies [6,9] using a uranium nitrate solution and the radioactive tracers. The uranium used in this
111 study was natural uranium. The atomic abundance ratio of ^{237}Np and ^{241}Am to ^{238}U in the tracer-doped
112 UO_2 was evaluated by α-particle spectrometry. The procedures of these radiochemical analyses have
113 been described previously [6]. The obtained atomic abundance of the tracer-doped UO_2 is presented
114 in Table 1. We observe that Am was present in trace amounts, which should not affect the chemistry
115 of the uranium compounds. The abundance of ^{237}Np was 0.16 atomic % of ^{238}U, which is close to the
116 composition of Np in the spent nuclear fuel produced by a commercial light water reactor (LWR). This
117 tracer-doped UO_2 was then used for the synthesis of the simulated MCCI debris by mixing it with
118 ZrO_2 and the concrete components ($CaCO_3$ and SiO_2), followed by heat treatment. Generally, CaO is
119 used as cementitious material to construct concrete structures. However, it is difficult to handle CaO
120 quantitatively in a laboratory experiment due to its strong hygroscopicity. To avoid extra uncertainty
121 caused by the hygroscopicity of CaO in the composition of the final products, $CaCO_3$ was employed
122 as the calcium source for the preparation of simulated MCCI debris in this study. $CaCO_3$ has low

123 hygroscopicity at room temperature. Moreover, it decomposes to CaO and CO_2 at 898 °C, which is
124 sufficiently lower than the designated heat treatment temperature for this study.
125 The appropriate amounts of the tracer-doped UO_2, ZrO_2 (Wako Pure Chemicals Ind., Ltd., Japan),
126 $CaCO_3$ (Wako Pure Chemicals Ind., Ltd. Japan), and SiO_2 (Wako Pure Chemicals Ind., Ltd., Japan)
127 powders were weighed to prepare the designated compositions as shown in Table 2. The specific
128 surface areas of the used UO_2 and ZrO_2 powder were 0.31 m^2/g and 2.87 m^2/g respectively, which
129 were measured by BET method in our previous study [9]. They were then well mixed and ground by
130 an automatic agate mortar (ANM-1000, Mizuho Machining Co., Ltd., Japan) for 30 minutes. For
131 comparison, simple UO_2 and UO_2-ZrO_2 mixture were also synthesized by the same heat treatment
132 procedure as that for the MCCI debris. The weighed sample was placed without compaction on a
133 platinum dish in the central part of a reaction tube made of quartz (for 1200 °C heat treatment) or
134 alumina (for 1600 °C heat treatment) surrounded by an electric furnace. It was heated for 1 hour at
135 1200 °C or 1600 °C at a 20 mL/min gas flow of 90 vol.% Ar + 10 vol.% H_2 or 98 vol.% Ar + 2 vol.%
136 O_2, respectively. The heating rates up to the designated temperatures are given in Table 2. The ultrapure
137 Ar (Grade 1), Ar + 10% H_2, and standard grade O_2 were purchased from Nihon Sanso Co., Ltd., Japan.
138 To investigate the effect of the redox atmosphere on the formed phases of the synthesized fuel debris,
139 we controlled the partial pressure of oxygen during the heat treatment by mixing 10% H_2 or 2% O_2
140 with ultrapure Ar gas. The log $P(O_2)$ values of the 90% Ar + 10% H_2 mixed gas and 98% Ar + 2% O_2
141 mixed gas were -13.7 and -1.7, respectively. In the case of heat treatment under reductive conditions
142 (10% H_2), the same 10% H_2 gas was introduced into the reaction tube during the temperature-

143 increasing and -decreasing processes. On the other hand, only ultrapure Ar gas was introduced into
144 the reaction tube during the temperature-increasing and -decreasing processes in the case of oxidative
145 heat treatment (2% O_2) to avoid extra oxidation of the samples. The initial composition and treatment
146 conditions of the simulated debris are listed in Table 2. At this study, we have particularly focused on
147 the effects of the initial elemental composition, the oxygen partial pressure, and the heat treatment
148 temperature on the formed phases of the simulated fuel debris. Therefore, the heat treatment time and
149 the gas flow rate were fixed to the constant values for the total of 14 samples.
150 After the heat treatment, the products were cooled down to room temperature by a rate of 5.6 ºC/min,
151 then, were pulverized by an agate mortar for powder X-ray diffractometry. The X-ray diffraction
152 (XRD) patterns of the products were measured by a Rigaku MiniFulex 600 diffractometer equipped
153 with the D/teX Ultra2 detector with Cu-Kα radiation at 40 kV and 15 mA. The diffraction data were
154 collected from 10° to 120° in 2θ with a step interval of 0.02° at a scan rate of 20°/min. The morphology
155 and element distribution mapping of the heat treatment products were obtained using a scanning
156 electron microscope (SEM, SU-1510, Hitachi, Japan) with an energy dispersive X-ray analyzer (EDX,
157 EMAX ENERGY EX-250, Horiba, Japan). For the SEM-EDX observation, the sample was placed on
158 an aluminum stage using a carbon double face tape. It was then coated with Au–Pd to increase the
159 conductivity using a magnetron sputter (MSP-1S, Vacuum Device Co., Ltd., Japan).
160
161 2.2 Leaching test of the radionuclides from the simulated MCCI debris
162 For the leaching tests, 40 mg of the simulated fuel debris was immersed without pulverization in 10

mL of Milli-Q water in a 50-mL polypropylene bottle; the solid to liquid ratio was 4.0 g/L. During the leaching tests, the sample bottles were slowly shaken in an air bath shaker continuously for 31 days at 25 °C. After shaking, the solution and residue were separated by suction filtration with a 0.45-μm-pore-size nitrocellulose membrane filter to determine the leaching ratios of the radionuclides in the solution. The filtrate was diluted to 100 mL with 1 M HNO_3, which was then used for α-spectrometry to measure the activities of the radionuclides in the soluble fraction. To determine the leaching ratios of each radionuclide, the activities of ^{238}U, ^{237}Np, and ^{241}Am in the filtrate solution were measured from the α peaks at 4.20, 4.79, and 5.49 MeV, respectively, in the spectra measured using a Si surface semiconductor detector (Model 7401, Canberra). The sample preparation for α-particle spectrometry of the filtrate solution was conducted using the samarium co-precipitation method developed by Mitsugashira et al. [14]. The details of the sample preparation procedure have been discussed in our previous studies [6,9].

3. Results and discussion

3.1 Characterization of the simulated MCCI debris

Figure 1 presents the XRD patterns of (a) the U-Ca-Si-O system's starting materials, (b) the product synthesized by the heat treatment at 1600 °C in 10% H_2, and (c) its magnified spectrum, along with the standard XRD patterns of the assigned phases from the Inorganic Crystal Structure Database (ICSD) [15]. The XRD patterns of the same system obtained by the heat treatment in 2% O_2 are shown in Figure 2; those of the U-Zr-Ca-Si-O system are shown in Figure 3 (heat treatment in 10% H_2) and

183 Figure 4 (heat treatment in 2% O_2) in the same manner as Figure 1. For comparison, the heat treatment
184 of simpler systems such as the U-O and U-Zr-O systems was also conducted under the same conditions
185 as the simulated MCCI debris. The XRD patterns of the obtained products are shown in the
186 supplementary materials: Figure S-1 (U-O system, heat treatment in 10% H_2), Figure S-2 (U-O system,
187 heat treatment in 2% O_2), Figure S-3 (U-Zr-O system, heat treatment in 10% H_2), and Figure S-4 (U-
188 Zr-O system, heat treatment in 2% O_2).

189 Figure S-1 shows that the UO_2 phase is very stable under heat treatment in 10% H_2 up to 1600 °C.
190 On the contrary, UO_2 is completely oxidized to U_3O_8 by the heat treatment in 2% O_2 at 1200 °C for 1
191 hour (Figure S-2), while U_3O_8 and UO_{2+x} co-exist in the product obtained by the heat treatment in 2%
192 O_2 at 1600 °C. Guéneau et al. reported that U_3O_8 decomposes to UO_{2+x} at temperatures of 1450 °C
193 and above under this oxygen partial pressure [16], which explains the existence of UO_{2+x} in our result
194 at 1600 °C while the co-existence of U_3O_8 phase in the product indicates that the U_3O_8 decomposition
195 reaction in our experiment did not reach the complete equilibrium state.

196 In the U-Zr-O system (heat treatment in 10% H_2), UO_2 and monoclinic ZrO_2 (m-ZrO_2) are stable,
197 and no phase change is observed at 1200 °C, as shown in Figure S-3 (b). On the other hand, a solid-
198 solution phase $(Zr_yU_{1-y})O_{2+x}$ is formed by the dissolution of Zr(IV) to UO_2 phase by the heat treatment
199 at 1600 °C, which can be inferred from the shift in the UO_2 peaks to higher 2θ angles (Figure S-3 (d)).
200 Due to the smaller ionic radius of Zr(IV) than that of U(IV) in the eight-coordination structure [17],
201 the XRD peaks of UO_2 shift to a higher angle when U(IV) is replaced by Zr(IV) in the UO_2 structure.
202 Kulkarni et al.[18] reported the lattice parameter change of the UO_2 phase with y and x as,

$$a = 5.4704 - 0.21x - 0.30y \quad (1)$$

for $Zr_yU_{1-y}O_{2+x}$, where a denotes expected lattice parameter (Å) of the solid solution. The lattice parameter of the product by the heat treatment at 1600 ºC in 10 % H_2 is calculated to be 5.4199 Å from the corresponding peaks in Figure S-3 (d) in the range of 2θ from 10° to 120° using "PDXL2" (RIGAKU). The x value of this product can be regarded as 0 since the heat treatment was conducted under the reducing condition (10 % H_2). Therefore, the y value of this product is calculated to be 0.17 by eq. (1). This y value clearly indicates the formation of a solid solution phase $Zr_{0.17}U_{0.83}O_2$ by the heat treatment at 1600 ºC, which is reasonable since the upper limit of y (= the solubility limit) at 1600 ºC is 0.4 according to the UO_2-ZrO_2 pseudo-binary diagram in the reducing condition [19].

In the oxidative (2% O_2) heat treatment of U-Zr-O sample, $(Zr_yU_{1-y})O_2$, m-ZrO_2, and t-ZrO_2 are formed both at 1200 and 1600 °C, as shown in Figure S-4. The U_3O_8 phase is observed only in the products of the 1200 °C heat treatment, which is explained by the above-mentioned decomposition of U_3O_8 stating at 1450 °C. At 1200 °C, the Zr(IV) dissolution to UO_2 phase is not observed in the reductive condition (in 10% H_2), while it is observed in the oxidative condition (in 2% O_2). This indicates that the progress of the solid-solution $(Zr_yU_{1-y})O_{2+x}$ formation depends not only on temperature but also on oxygen potential, and oxidative condition is favorable for it. The lattice parameter of the product by the heat treatment at 1600 ºC in 2 % O_2 is calculated to be 5.2854 Å from the corresponding peaks in Figure S-4 (d). Since the heat treatment of this product was done in the oxidative condition, the x value in $(Zr_yU_{1-y})O_{2+x}$ is larger than 0. The oxidation of UO_2 doped with zirconium seems to proceed via the sequence: $MO_2 \rightarrow MO_{2+x} \rightarrow M_4O_9 \rightarrow U_3O_8 + MO_{2+x} + ZrO_2 \rightarrow$

223 U_3O_8 + ZrO_2 (M = U + Zr), therefore, the x value limit should be 0.25. Based on this assumption, the
224 obtained lattice parameter 5.2854 Å and x value 0.25 are substituted for *a* and x in Eq.(1), then, 0.44
225 is obtained as y value of the product by the heat treatment at 1600 ºC in 2% O_2. This y value is larger
226 than the above mentioned y value of the product obtained in the reducing condition at 1600 ºC, and is
227 close to the reported solubility limit 0.4 of Zr in $(Zr_yU_{1-y})O_{2+x}$ by Cohen et al.[19], which clearly
228 indicates the more progress of the solid solution formation in the oxidative condition than in the
229 reducing condition. It should be noted here that the reported solubility limit by Cohen et al. is for the
230 reducing condition. The obtained result for the U-Zr-O system at 1200 °C is quite comparable to the
231 results of our previous work [9].
232 In the simulated MCCI debris (U-Ca-Si-O system) obtained by the heat treatment in 10% H_2 at
233 1600 °C, only the UO_2 phase is confirmed in the XRD pattern of the products and no peak shift is
234 observed (Figure 1), indicating that UO_2 does not interact with Ca or Si under this condition. On the
235 contrary, under the heat treatment in 2% O_2 at 1600 °C, a remarkable peak shift in the UO_2 phase is
236 observed in the XRD pattern of the product of U-Ca-Si-O system (Figure 2). This peak shift indicates
237 that the U in UO_2 structure could be displaced randomly by a smaller size cation Ca(II) into the UO_2
238 structure and form a solid-solution $(Ca_yU_{1-y})O_{2+x}$ phase. To confirm the $(Ca_yU_{1-y})O_{2+x}$ phase formation
239 by this oxidative heat treatment, SEM-EDX analysis was conducted on this sample. The obtained SEM
240 image, measured by the backscattered electron (BSE) mode, and the elemental mappings for U, Ca,
241 and Si are shown in Figure 5. The U-rich part in the particle appears bright in the SEM image (Figure
242 5 (a)), while the Si-rich part seems dark. The distribution of U (Figure 5 (b)) and that of Si (Figure 5

(d)) are clearly separated from each other, while the Ca distribution in Figure 5 (c) shows an overlapping with that of U for this particle. EDX composition analysis indicated that the element composition in the U-rich area was U : Ca : Si = 73 : 24 : 3 in atomic ratio, while that in the Si-rich area was U : Ca : Si = 0.4 : 0.0 : 99.6. This result is an evidence that the $(Ca_yU_{1-y})O_{2+x}$ phase formed in this sample and caused the remarkable peak shift in XRD pattern of the UO_2 phase in the XRD pattern shown in Figure 2. In the study of the interaction between the (U, Zr)O_2 simulated debris and sea salt deposits in the temperature range of 815 to 1395 °C in Ar atmosphere, Takano et al. observed Ca diffusion into a cubic UO_2 matrix, resulting in the formation of a solid-solution $(Ca_yU_{1-y})O_{2+x}$ phase [20]. This supports our interpretation of the formed phases of the simulated MCCI debris (U-Ca-Si-O system) in this study. The optical image of the simulated MCCI debris obtained by the heat treatment in 2% O_2 at 1600 °C is presented in Figure 6 with the image before heat treatment. The product (Figure 6 (b)) appears to be a black-glossy in a melted state, which is completely different from the initial material showing brown color and powder state. This glossy surface was not observed in the MCCI debris (U-Ca-Si-O system) synthesized by reductive (10% H_2) heat treatment at 1600 °C. The other products without glass like material formation were powder-like state. To understand what led to this glossy surface on the simulated MCCI debris obtained by the heat treatment in 2% O_2 at 1600 °C, the same treatment was conducted for a simple mixture of $CaCO_3$ and SiO_2 (1:1 in molecular ratio) without UO_2. The optical images of the initial material and the product are presented in Figure S-5. We observe that the fine white powder changes to clear and glass-like particles by the heat treatment. The CaO-SiO_2 pseudo binary phase equilibrium diagram calculated by Rannikko [21] indicates that Si-Ca-O

liquid phase is thermodynamically stable at 1600 °C in this system. Since a liquid phase formation at high temperature is necessary to form a glass phase after cooling, the phase equilibrium information supports the observed glass phase formation in Figure S-5. As a result, this simple experiment revealed that the glass-like material, which originated from the Ca and SiO_2 mixture, resulted in the glossy surface on the simulated MCCI debris. Based on the SEM-EDX result presented in Figure 5 and Figure S-5, it is concluded that the solid-solution phase $(Ca_yU_{1-y})O_{2+x}$ was coated or covered by a silica glass in the simulated MCCI debris synthesized by the heat treatment in 2% O_2 at 1600 °C, which is believed to be an important characteristic state of MCCI debris.

In the cladding material-added simulated MCCI debris (U-Zr-Ca-Si-O system) synthesized by the heat treatment in 10% H_2 at 1200 °C, UO_2 and m-ZrO_2 were stable, and no phase change was observed in the XRD pattern, as shown in Figure 3 (b). On the other hand, the XRD pattern of the product at 1600 °C (Figure 3 (d)) shows that two solid-solution phases, i.e., $(Zr_yU_{1-y})O_{2+x}$ and $Ca_{0.15}Zr_{0.85}O_{1.85}$, were formed by the dissolution of Zr(IV) to UO_2 phase and Ca(II) to t-ZrO_2 phase, respectively; this can be inferred from the shift of the typical UO_2 peaks and t-ZrO_2 peaks in Figure 3 (d). The formation of $(Zr_yU_{1-y})O_{2+x}$ in this sample is comparable with the result of the heat treatment in 10% H_2 at 1600 °C for the U-Zr-O system, as shown in Figure S-3 (d) and Table 2. For the oxidative heat treatment in 2% O_2, a further peak shift in the UO_2 phase is observed in the XRD patterns of the Zr-added simulated MCCI debris (U-Zr-Ca-Si-O system) as shown in Figure 4, indicating further progress of the solid-solution formation in comparison with the product obtained by the reductive heat treatment. The UO_2 solid-solution, U_3O_8, and t-ZrO_2 phases are identified in the XRD pattern of the product of the U-Zr-

283 Ca-Si-O system treated in 2% O_2 at 1200 °C (Figure 4(b)), while only the UO_2 solid-solution phase is
284 identified in that for the product at 1600 °C (Figure 4(d)). The appearance of the Zr-added simulated
285 MCCI debris synthesized by the oxidative treatment at 1600 °C is very similar to the MCCI debris (U-
286 Ca-Si-O system) shown in Figure 6(b), i.e., black-glossy melt, while those glossy surfaces are not
287 observed in the product at 1200 °C. The SEM image of the U-Zr-Ca-Si-O debris particles treated in
288 2% O_2 at 1600 °C and the elemental mappings for U, Zr, Ca, and Si are shown in Figure 7. The Zr
289 distribution is well-overlapped with the U distribution, while the Si distribution is separated from those
290 of U and Zr. It should be noted that Ca was distributed in both the U-Zr-rich area and Si-rich area in
291 the particle. The EDX composition analysis indicates that the element composition in the U-Zr-rich
292 area was U : Zr : Ca : Si = 41 : 42 : 15 : 2 in atomic ratio, while that in the Si-rich area was U : Zr :
293 Ca : Si = 2 : 14 : 39 : 45. Further, no peak corresponding to the $CaSiO_3$ phase is observed. These results
294 indicate that the particle shown in Figure 7 (a) consisted of a solid-solution phase $(Ca_yZr_xU_{1-y-z})O_{2+x}$
295 and an amorphous calcium-silicate phase. The formation of the $(Ca_yZr_zU_{1-y-z})O_{2+x}$ phase in U-Zr-Ca-
296 Si-O system is reasonably supported by the results of the above-mentioned simpler systems, i.e.,
297 $(Zr_yU_{1-y})O_{2+x}$ and $(Ca_yU_{1-y})O_{2+x}$ phases were formed by the same oxidative heat treatment in U-Zr-O
298 and U-Ca-Si-O systems, respectively. Besides, the amorphous calcium-silicate phase existing in the
299 Zr-added simulated MCCI debris by the oxidative treatment at 1600 °C is believed to be silica glass,
300 because of the above discussion on the Ca-SiO_2 interaction products shown in Figure S-5 by the same
301 oxidative heat treatment. It is believed that this silica glass phase leads to the glossy surface in the
302 simulated MCCI debris.

303 The identified phases from the results and discussion in this section are listed in the extreme right
304 column of Table 2 for each sample.
305
306 3.2 Leaching behavior of actinides from the simulated MCCI debris
307 To investigate the effect of the composition of MCCI debris and the redox conditions during debris
308 formation on the leaching behavior of the actinides, leaching tests of the simulated MCCI debris and
309 other simpler samples such as the U-Zr-O system were conducted in water at 25 °C for 31 days. The
310 leaching ratio of an element 'M' (= R_M (%)) is defined by Eq. (1).
311 $$R_M(\%) = \frac{A^M_{sol.}(\mathrm{Bq})}{A^M_{total}(Bq)} \times 100 \quad (1)$$
312 $A^M_{sol.}$ expresses the radioactivity of the element 'M' dissolved in the solution phase by the leaching
313 test (the soluble fraction); this was measured by α-particle (^{238}U, ^{237}Np, and ^{241}Am) spectrometry of
314 the filtrate solution separated from the residue by the above-mentioned suction filtration. A^M_{total}
315 expresses the total radioactivity of the element 'M' initially in the simulated MCCI debris before the
316 leaching test; this was calculated from the contained weight of the tracer-doped UO_2 in the debris and
317 the atomic abundance of Np and Am to U in the tracer-doped UO_2 given in Table 1.
318 First of all, it should be noted that the observed leaching of the actinides (U, Np, and Am) from the
319 simulated debris was very limited and less than 0.4% for all experimental conditions in this study. The
320 effect of the concrete components (Ca and SiO_2) in the debris on actinide leaching was investigated
321 by comparing the leaching ratios from the U-Zr-O system debris and those from the MCCI debris (U-
322 Zr-Ca-Si-O system) to water, where the used debris were synthesized at 1600 °C. The results of these

323 leaching tests are shown in Figure 8, where the red line indicates the detection limit of the leaching
324 ratio by the experiment (= 0.01%). The pH values after the leaching tests are indicated in the graphs
325 in Figures 8-10 as "$pH_{fin.}$". A significant increase in pH is observed only for the leaching test using the
326 U-Zr-Ca-Si-O debris synthesized in the reductive atmosphere, where the alkaline source is believed to
327 be CaO in the debris formed by the decomposition of $CaCO_3$. This pH increase is not observed for the
328 leaching test using the MCCI debris synthesized in the oxidative atmosphere, indicating that the Ca in
329 the debris has been almost completely consumed by the formation of the solid-solution phase with
330 UO_2 and/or by the formation of the glass-like material with SiO_2. It is obvious that the leaching of the
331 actinides from the debris synthesized in oxidative condition (Figure 8(b)) is suppressed in comparison
332 with that from the debris synthesized in reductive condition (Figure 8(a)), regardless of the existence
333 of the concrete components. This result can be explained by the progress of the formation of the solid-
334 solution phases, $(Zr_yU_{1-y})O_{2+x}$ or $(Ca_yZr_zU_{1-y-z})O_{2+x}$, by the oxidative heat treatment in comparison
335 with that by the reductive treatment, as shown in Table 2. Since the dissolution of $U^{IV}O_2(s)$ is the
336 oxidative dissolution to uranyl(VI) ion ($U^{VI}O_2^{2+}$) by dissolved oxygen or other oxidants, the matrix is
337 more stabilized when a part of U(IV) in the UO_2 structure is substituted by a redox insensitive cation
338 such as Zr(IV) or Ca(II). It should be noted that the existence of the concrete components (CaO and
339 SiO_2) in the debris remarkably suppressed the actinide leaching. As described in Section 3.1, the
340 simulated MCCI debris synthesized at 1600 °C in oxidative condition were coated by a glossy glass-
341 like material as shown in Figure 6 and Figure S-5. Owing to this glass-like coating, it seems that the
342 surface area of the debris contacting on the water phase decreased and the actinides were covered by

343 the glass. As a result, the actinide leaching from the simulated MCCI debris is effectively suppressed
344 in comparison with that from the U-Zr-O system debris. The reported amount of actinides leached out
345 from the real debris in the Fukushima NPP is so far very limited. For example, [^{235}U] = (1.8 ± 0.2)
346 ×10^{-5} Bq/cm^3 ≅ 2.3 × 10^{-7} g/L, [^{238}U] = (1.7 ± 0.1) × 10^{-4} Bq/cm^3 ≅ 1.4 × 10^{-5} g/L, and [^{241}Am] =
347 (2.7 ± 0.1) × 10^{-1} Bq/cm^3 ≅ 2.1 × 10^{-9} g/L in a retained water sample (LI-3RB5-1) from the PCV of
348 unit-3 [22], in which the formation of the glass-like material by the MCCI as shown in Figure 6 and
349 Figure S-5 may play an important role in the effective suppression of the actinide leaching.
350 The effect of the cladding material Zr in the debris on the actinide leaching was investigated by
351 comparing the leaching ratios in the U-Ca-Si-O system debris and those in the U-Zr-Ca-Si-O debris
352 to water, where the used debris were synthesized at 1600 °C. The results of these leaching tests are
353 shown in Figure 9. Due to the extremely low actinide leaching (i.e., near the detection limit or lower),
354 the effect of Zr in the debris is not observed in the leaching test using the debris synthesized in
355 oxidative condition, as shown in Figure 9 (b). This seems a reasonable result since both the U-Ca-Si-
356 O system debris and the U-Zr-Ca-Si-O debris synthesized in oxidative condition at 1600 °C were
357 coated by the glossy glass-like material as discussed in Section 3.1; therefore, the actinide leaching
358 was effectively suppressed. On the contrary, the Zr effect is clearly observed in the leaching of U and
359 Np from the debris synthesized in the reductive condition (Figure 9 (a)), where the glossy glass-like
360 material was not formed in the MCCI debris. In this leaching test, more than 0.2% of U and Np were
361 leached out from the U-Ca-Si-O debris, while 0.01% (i.e., the detection limit level) or a lower amount
362 of U and Np were leached out from the U-Zr-Ca-Si-O debris. As described in Section 3.1 and

363 summarized in Table 2, no solid-solution phase was formed in the U-Ca-Si-O debris synthesized under
364 the reductive condition; on the other hand, a solid-solution phase $(Zr_yU_{1-y})O_{2+x}$ was formed in the U-
365 Zr-Ca-Si-O debris under the same heat treatment. This Zr substitution of U in the UO_2 matrix
366 chemically stabilized the simulated debris so that the actinide leaching was remarkably suppressed.
367 Finally, the effect of the heat treatment temperature on the actinide leaching was investigated by
368 comparing the leaching ratios from the Zr-added MCCI (U-Zr-Ca-Si-O) debris synthesized at 1200
369 and 1600 °C. The results are shown in Figure 10. Due to the very low leaching ratios (i.e., the level of
370 the detection limit or lower, as shown in Figure 10(a)), the heat treatment temperature effect cannot
371 be discussed for the leaching from the debris synthesized under the reductive condition (10% H_2). On
372 the contrary, a remarkable suppression effect on the actinide leaching due to the heat treatment
373 temperature is observed in Figure 10(b), where the leaching ratios from the debris synthesized under
374 oxidative condition (2% O_2) at 1200 and 1600 °C are compared. The leaching ratios of U and Np from
375 the debris synthesized at 1200 °C are obviously higher than those from the debris synthesized at
376 1600 °C. This result can be explained by the difference in the matrix phases in the debris shown in
377 Table 2: a part of the matrix of the debris synthesized at 1200 °C is U_3O_8 that has a higher solubility
378 than UO_2, while the main matrix of the debris synthesized at 1600 °C is a solid-solution phase
379 $(Ca_yZr_zU_{1-y-z})O_{2+x}$. Since Ca(II) and Zr(IV) are redox insensitive, the dissolution of these elements to
380 the UO_2 matrix chemically stabilizes the debris for the leaching. In addition, due to the formation of
381 the glass like coating on the surface, the surface area of the debris synthesized at 1600 °C remarkably
382 decreased compared with the debris synthesized at 1200 °C, which is also believed to suppress the

383 actinide leaching effectively. The same heat treatment temperature effect on the actinide leaching is
384 observed in the leaching test of the simpler system, i.e., the U-Zr-O debris, synthesized under the
385 oxidative condition.
386
387 **4. Conclusions**
388 To better understand the chemical properties of the MCCI debris generated by the Fukushima Daiichi
389 NPP accident, we investigated the structure and the leaching behavior of U-O, U-Zr-O, U-Ca-Si-O,
390 and U-Zr-Ca-Si-O systems of simulated fuel debris in which the actinide tracers ^{237}Np and ^{241}Am were
391 doped. The debris were synthesized under reductive and oxidative atmospheres at 1200 and 1600 °C.
392 The characterization results of the synthesized debris revealed that the crystal structure of the debris
393 was changed by the composition, atmosphere, and temperature during the synthesis. Therefore, the
394 leaching behavior from the debris was sensitive to the synthesis condition, although the actinide
395 leaching ratios itself were very limited and less than 0.4% for all the experiments in this study. The
396 existence of the concrete components (CaO and SiO_2) in the debris remarkably suppressed the actinide
397 leaching by forming a glass-like coating on the debris, which is supposed to play an important role in
398 the leaching of the actinides from the real MCCI debris in the Fukushima NPP. Moreover, it was
399 revealed that Zr and Ca formed solid-solution phases such as $(Zr_yU_{1-y})O_{2+x}$, $(Ca_yU_{1-y})O_{2+x}$, and
400 $(Ca_yZr_zU_{1-y-z})O_{2+x}$ which stabilized the matrix of the simulated debris. In consequence, the actinide
401 leaching from the debris was suppressed. Since the effects of the initial elemental composition, the
402 oxygen partial pressure, and the heat treatment temperature on the formed phases of the simulated fuel

403 debris were particularly focused in this study, the heat treatment time and other conditions were fixed
404 to be constant. It seems that the time dependence of the heat treatment on the phase relation of the
405 debris is an important topic to be investigated. That will be studied in our future work.
406 Based on these experimental results, the formed MCCI debris in the Fukushima Daiichi NPP is
407 expected to be chemically more stable to the leaching of the actinides (U, Np, and Am) than that from
408 normal spent nuclear fuels, at least within the range of the conditions examined in this study. These
409 results could assist TEPCO's future action plan for the decommissioning of the damaged reactors.
410
411 ***Acknowledgments***
412 This work was supported by JSPS KAKENHI (grant number 16H02447). A part of this work was
413 performed under the Research Program for CORE lab of "Dynamic Alliance for Open Innovation
414 Bridging Human, Environment and Materials" in "Network Joint Research Center for Materials and
415 Devices."
416
417 **References**
418 [1] Nuclear Accident Response Office, Agency for Natural Resources and Energy, Important Stories
419 on Decommissioning 2018, Fukushima Daiichi Nuclear Power Station, now and in the future,
420 Tokyo: Japanese Ministry of Economy, Trade and Industry (METI); March, 2018. (2018) Available
421 from:
422 https://www.meti.go.jp/english/earthquake/nuclear/decommissioning/pdf/20180827_roadmap.pd

f

[2] Tokyo Electric Power Company Holdings, Inc., Released meeting materials at Secretariat meeting of the Team for Countermeasures for Decommissioning and Contaminated Water Treatment (in Japanese). Tokyo: Japanese Ministry of Economy, Trade and Industry (METI); May 30, 2019. (2019) Available from: https://www4.tepco.co.jp/decommission/information/committee/roadmap_progress/pdf/2019/d190530_07-j.pdf

[3] Tokyo Electric Power Company, Reactor imaging technology for fuel debris detection by cosmic ray muon, Measurement status report in Unit-1, Tokyo: IRID (International Research Institute for Nuclear Decommissioning); March 19, 2015. (2015) Available from: http://irid.or.jp/wp-content/uploads/2015/03/20150319_e.pdf

[4] M. Nagano, S. Sekita, Muon Tomography Scan of Nuclear Reactor (in Japanese), IEEJ journal, 138, 522-524 (2018)

[5] N. Sato, A. Kirishima, T. Sasaki, Behavior of fuel and structural materials in severely damaged reactors, Proceedings of CIMTEC 2014, Advances in Science and Technology, 6th Forum on New Materials, Part B, 93–96, Trans. Tech. Pub. Inc. (2014).

[6] A. Kirishima, M. Hirano, T. Sasaki, N. Sato, Leaching of actinide elements from simulated fuel debris into seawater, Journal of Nuclear Science and Technology, 52, 1240–1246 (2015)

[7] T. Sasaki, Y. Takeno, T. Kobayashi, A. Kirishima, N. Sato, Leaching test of gamma-emitting Cs, Ru, Zr, and U from neutronirradiated UO_2/ZrO_2 solid solutions in non-filtered surface seawater,

443 Journal of Nuclear Science and Technology, 52, 147–151 (2015).

444 [8] T. Sasaki, Y. Takeno, T. Kobayashi, A. Kirishima, N. Sato, Leaching behavior of gamma-emitting

445 fission products and Np from neutron-irradiated UO_2–ZrO_2 solid solutions in non-filtered surface

446 seawater, Journal of Nuclear Science and Technology, 53, 303–311 (2016).

447 [9] A. Kirishima, M. Hirano, D. Akiyama, T. Sasaki, N. Sato, Study on the leaching behavior of

448 actinides from nuclear fuel debris, J. Nucl. Mater. 502, 169-176 (2018).

449 [10] D. Akiyama, H. Akiyama, A. Uehara, A. Kirishima, N. Sato, Phase analysis of uranium oxides

450 after reaction with stainless steel components and ZrO_2 at high temperature by XRD, XAFS, and

451 SEM/EDX, J. Nucl. Mater. 520, 27-33 (2019).

452 [11] T. Kitagaki, K. Yano, H. Ogino, T. Washiya, Thermodynamic evaluation of the solidification

453 phase of molten core-concrete under estimated Fukushima Daiichi nuclear power plant accident

454 conditions, J. Nucl. Mater. 486, 206-215 (2017)

455 [12] M. Hidaka, T. Fujii, T. Sakai, Improvement of molten core-concrete interaction model in debris

456 spreading analysis module with consideration of concrete degradation by heat, Journal of Nuclear

457 Science and Technology, 53(9), 1260-127 (2016)

458 [13] M. Hidaka, T. Fujii, T. Sakai, Development of the models for advection-diffusion of eroded

459 concrete into debris and concrete volume reduction in molten core-concrete interactions, Journal

460 of Nuclear Science and Technology, 54(9), 977-990 (2017)

461 [14] H. Kikunaga, Y. Kasamatsu, K. Takamiya, T. Ohtsuki, H. Yuki, A. Yokoyama, T. Nakanishi, T.

462 Mitsugashira, Development of a rapid source preparation method for high-resolution α-particle

463 spectrometry, Applied Radiation and Isotopes, 67, 539–543 (2009)

464 [15] G. Bergerhoff, I. D. Brown, in “Crystallographic Databases“, F.H. Allen et al. (Hrsg.), Chester,

465 International Union of Crystallography, (1987)

466 [16] C. Guéneau, M. Baichi, D. Labroche, C. Chatillon, B. Sundman, Thermodynamic assessment of

467 the uranium–oxygen system, Journal of Nuclear Materials, 304, 161-175 (2002)

468 [17] Y. Marcus, Ion Properties. Marcel Dekker, Inc, New York, (1997).

469 [18] N. K. Kulkarni, K. Krishnan, U. M. Kasar, S. K. Raksit, S. K. Sali, S. K. Aggarwal, Thermal

470 Studies on Fluorite Type $Zr_yU_{1-y}O_2$ Solid Solutions, J. Nuclear Materials, 384 (2009) 81-86.

471 [19] I. Cohen, B. E. Schaner, A Metallographic and X-ray Study of the UO_2-ZrO_2 System, J. Nuclear

472 Materials, 9 (1963)18-52.

473 [20] M. Takano, T. Nishi, High-temperature reaction between sea salt deposit and $(U,Zr)O_2$ simulated

474 corium debris, Journal of Nuclear Materials, 443, 32-39 (2013).

475 [21] H. Rannikko, A thermodynamic assessment of the Cu-O-CaO-SiO_2 system, Acta polytech. Scand.

476 Chem. Technol. series, 229, 1-78 (1995).

477 [22] Japan atomic Energy agency (in Japanese), in: Released Meeting Materials at Secretariat Meeting

478 of the Team for Countermeasures for Decommissioning and Contaminated Water Treatment,

479 Japanese Ministry of Economy, Trade and Industry (METI), Tokyo, February 24, 2017 (2017)

480 Available from:

481 http://www.meti.go.jp/earthquake/nuclear/decommissioning/committee/osensuitaisakuteam/2017

482 /02/3-04-04.pdf.

Table 1. The atomic abundance of Np, and Am to U in the synthesized tracer-doped UO_2.

Element	^{238}U	^{237}Np	^{241}Am
Abundance to ^{238}U	1	1.6×10^{-3}	1.4×10^{-7}

Table 2. Composition, treatment condition, and identified phases of the synthesized simulated debris

Type	Composition (molar ratio)	Temp. (℃)	Atmosphere	Heating duration (h)	Heating and cooling rates	Identified phases
U-O system	UO_2	1200	10 % H_2	1.0	25 to 1000 ºC : 5.6 ºC/min 1000 to 1300 ºC : 5.0 ºC/min 1300 to 1600 ºC : 3.0 ºC/min (Cooling rate: 5.6 ºC/min)	UO_2
			2 % O_2			U_3O_8
		1600	10 % H_2			UO_2
			2 % O_2			U_3O_8, UO_{2+x}
U-Zr-O system	UO_2 : ZrO_2 =1:1	1200	10 % H_2			UO_2, m-ZrO_2,
			2 % O_2			$(Zr_yU_{1-y})O_2$, U_3O_8, m-ZrO_2, t-ZrO_2
		1600	10 % H_2			UO_2, m-ZrO_2, $(Zr_yU_{1-y})O_2$, t-ZrO_2
			2 % O_2			$(Zr_yU_{1-y})O_2$, m-ZrO_2, t- ZrO_2
U-Ca-Si-O system	UO_2 : $CaCO_3$: SiO_2 =1:1:1	1600	10 % H_2			UO_2
			2 % O_2			$(Ca_yU_{1-y})O_2$
U-Zr-Ca-Si-O system	UO_2 : ZrO_2 : $CaCO_3$: SiO_2 =1:1:1:1	1200	10 % H_2			UO_2, m-ZrO_2
			2 % O_2			$(Ca_zZr_yU_{1-y-z})O_2$, U_3O_8, t-ZrO_2
		1600	10 % H_2			$(Zr_yU_{1-y})O_2$, $Ca_{0.15}Zr_{0.85}O_{1.85}$
			2 % O_2			$(Ca_zZr_yU_{1-y-z})O_2$

Figure captions

Figure 1. XRD patterns of the simulated MCCI debris (U-Ca-Si-O system) synthesized in 10% H_2. (UO_2 : $CaCO_3$: SiO_2 =1:1:1)..

Figure 2. XRD patterns of the simulated MCCI debris (U-Ca-Si-O system) synthesized in 2% O_2. (UO_2 : $CaCO_3$: SiO_2 =1:1:1).

Figure 3. XRD patterns of the Zr added MCCI debris (U-Zr-Ca-Si-O system) synthesized in 10% H_2. (UO_2 : ZrO_2 : $CaCO_3$: SiO_2 =1:1:1:1).

Figure 4. XRD patterns of the Zr added MCCI debris (U-Zr-Ca-Si-O system) synthesized in 2% O_2. (UO_2 : ZrO_2 : $CaCO_3$: SiO_2 =1:1:1:1).

Figure 5. SEM image, and elemental mappings by EDX of the simulated MCCI debris (U-Ca-Si-O system) synthesized in 2% O_2 at 1600 ºC. (UO_2 : $CaCO_3$: SiO_2 = 1:1:1).

Figure 6. Optical images of the simulated MCCI debris (U-Ca-Si-O system) synthesized by 2% O_2 heat treatment at 1600 ºC.

Figure 7. SEM image, and elemental mappings by EDX of the Zr added MCCI debris (U-Zr-Ca-Si-O system) synthesized in 2% O_2 at 1600 ºC. (UO_2 : ZrO_2 : $CaCO_3$: SiO_2 =1:1:1:1).

Figure 8. A comparison of the leaching ratios of the actinides between from U-Zr-O debris and from Zr added MCCI (U-Zr-Ca-Si-O) debris. (a): Debris synthesized in 10 % H_2 at 1600 ºC, (b): Debris synthesized in 2 % O_2 at 1600 ºC,

Leaching test : for 31 days at 25 ºC

Figure 9. A comparison of the leaching ratios of the actinides between from the MCCI

(U-Ca-Si-O) debris and from the Zr added MCCI (U-Zr-Ca-Si-O) debris. (a): Debris synthesized in 10 % H_2 at 1600 ºC, (b): Debris synthesized in 2 % O_2 at 1600 ºC,

Leaching test : for 31 days at 25 ºC

Figure 10. A comparison of the leaching ratios of the actinides from the Zr added MCCI (U-Zr-Ca-Si-O) debris synthesized at 1200 ºC and 1600 ºC.
(a): Debris synthesized in 10 % H_2, (b): Debris synthesized in 2 % O_2,
Leaching test : for 31 days at 25 ºC

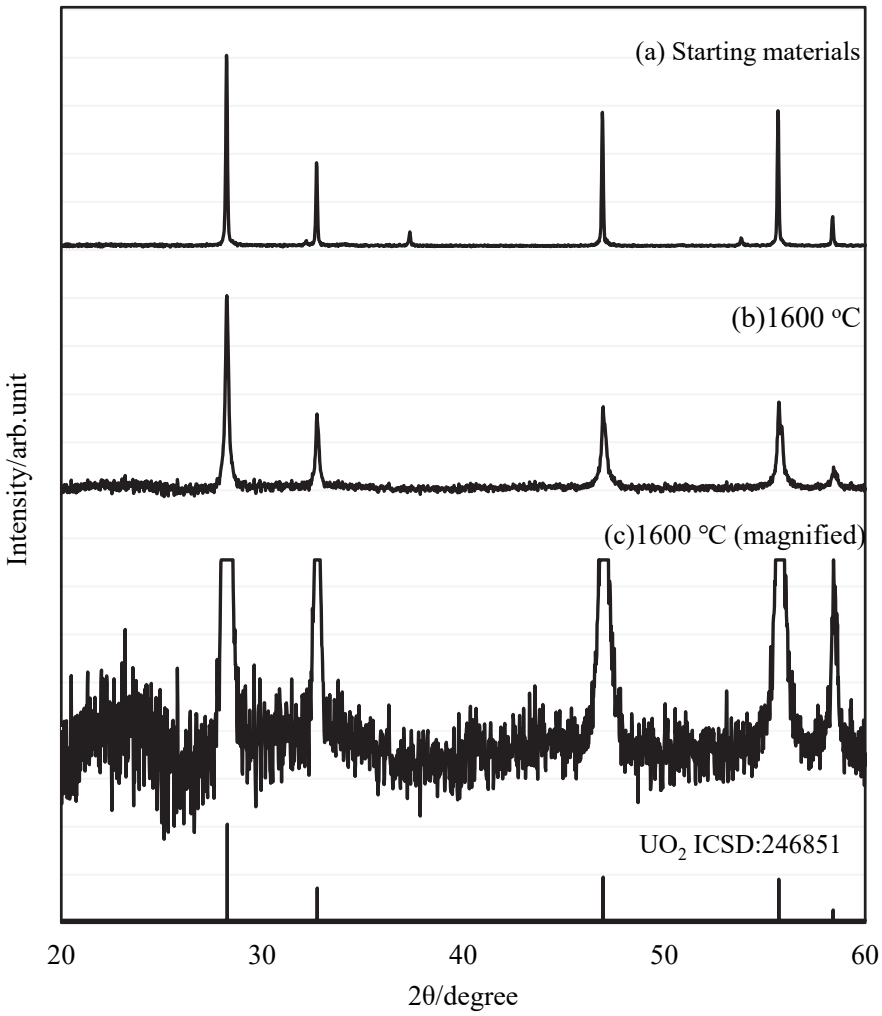

Figure 1. XRD patterns of the simulated MCCI debris (U-Ca-Si-O system) synthesized in 10% H_2 (UO_2 : $CaCO_3$: SiO_2 = 1 : 1 : 1).

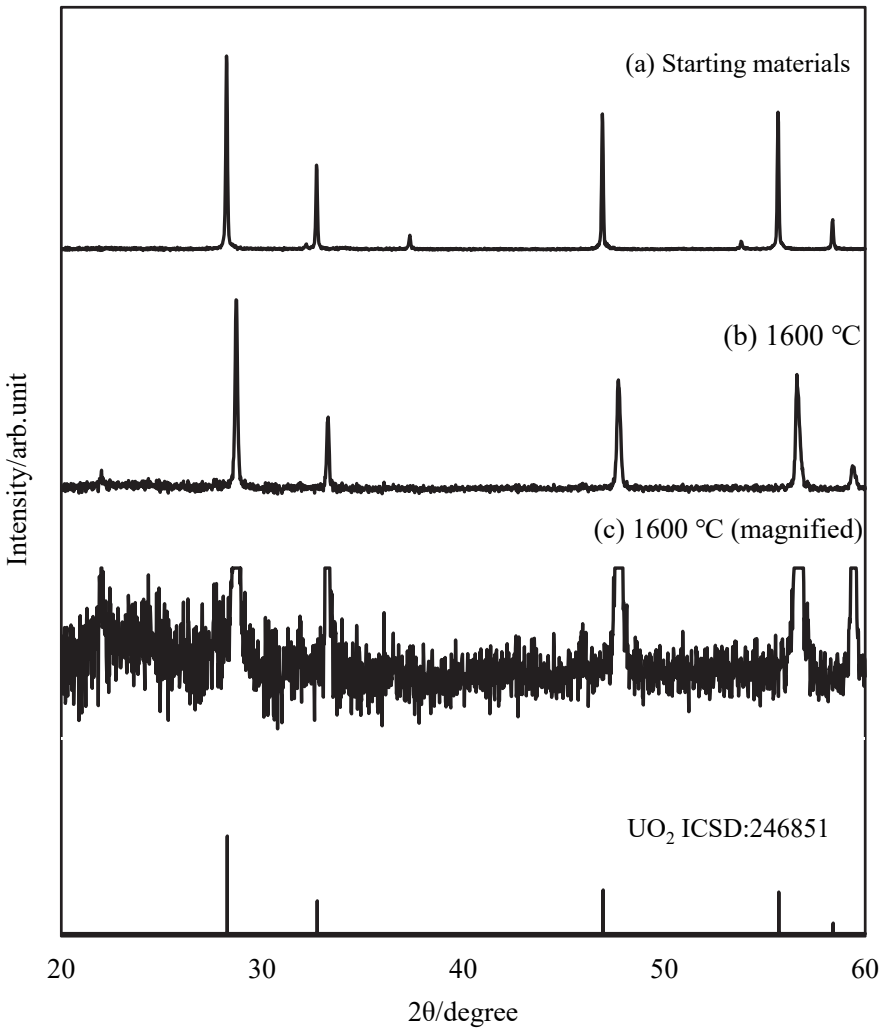

Figure 2. XRD patterns of the simulated MCCI debris (U-Ca-Si-O system) synthesized in 2% O_2 (UO_2 : $CaCO_3$: SiO_2 = 1 : 1 : 1).

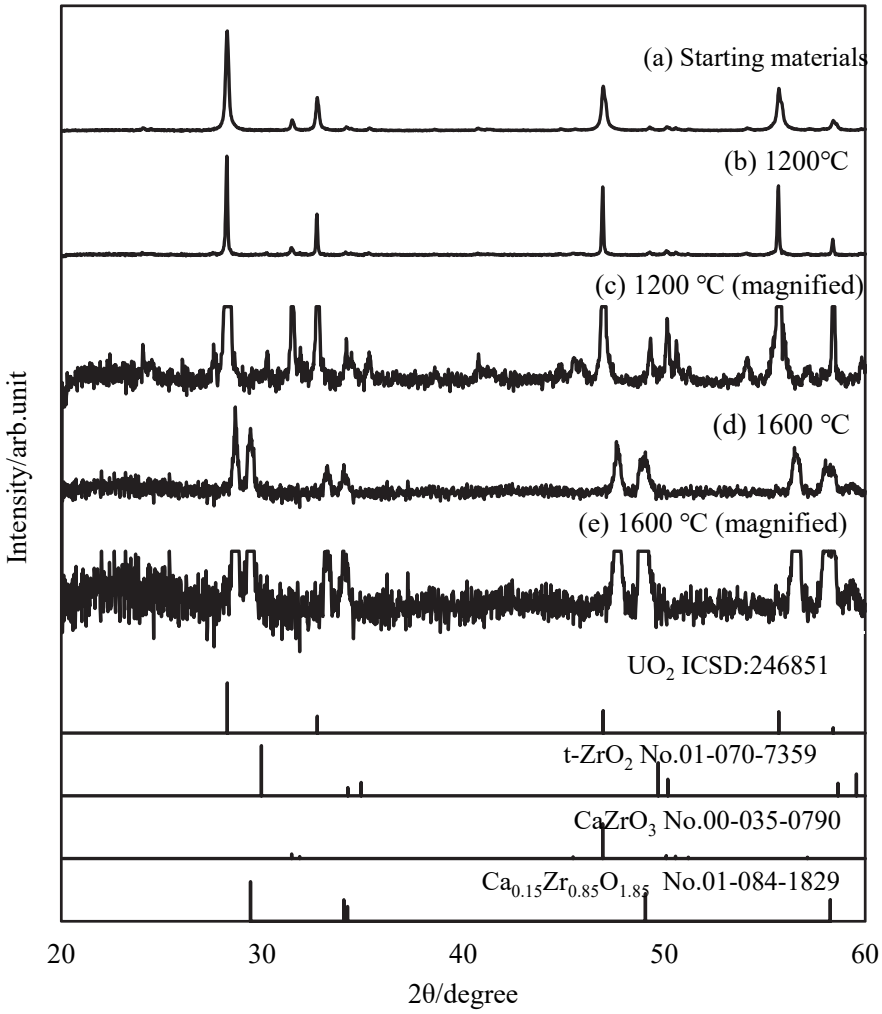

Figure 3. XRD patterns of the Zr-added MCCI debris (U-Zr-Ca-Si-O system) synthesized in 10% H_2 (UO_2 : ZrO_2 : $CaCO_3$: SiO_2 = 1 : 1 : 1 : 1).

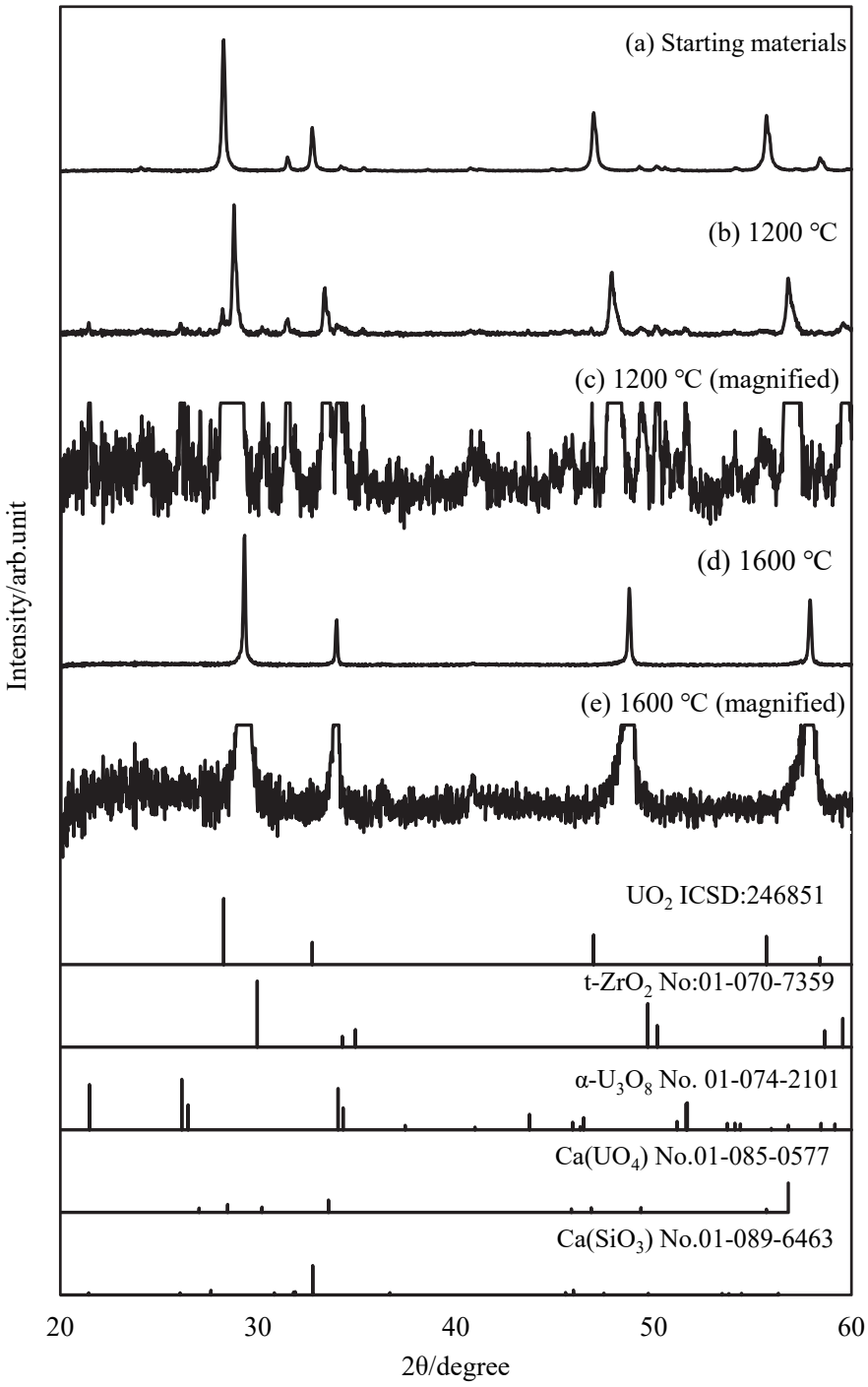

Figure 4. XRD patterns of the Zr-added MCCI debris (U-Zr-Ca-Si-O system) synthesized in 2% O_2 (UO_2 : ZrO_2 : $CaCO_3$: SiO_2 = 1 : 1 : 1 : 1).

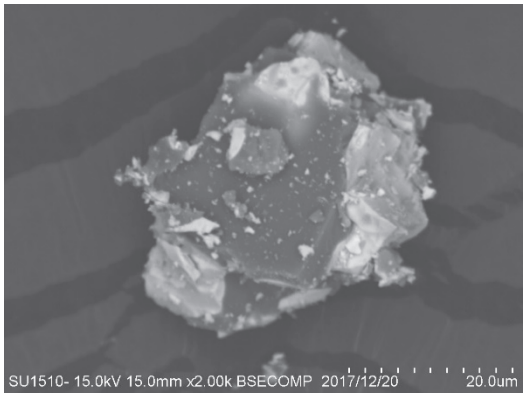

(a) SEM image by backscattered electron mode.

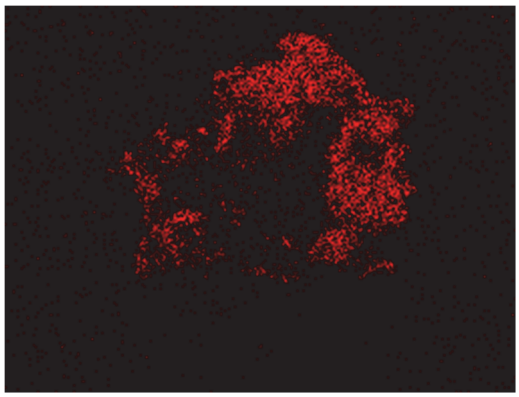

(b) U distribution mapping.

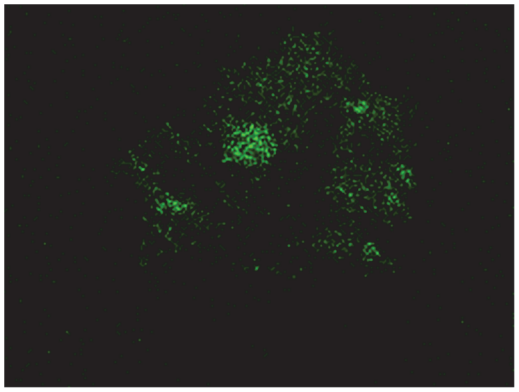

(c) Ca distribution mapping.

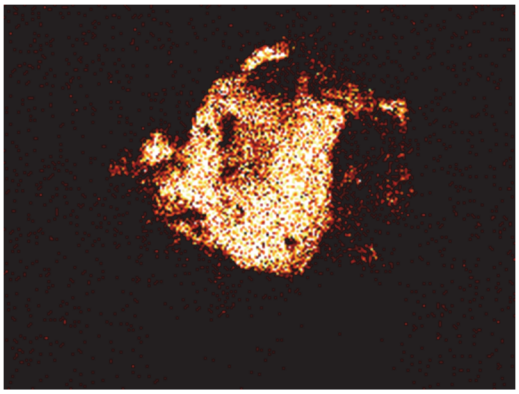

(d) Si distribution mapping.

Figure 5. SEM image and elemental mappings by EDX of the simulated MCCI debris (U-Ca-Si-O system) synthesized in 2% O_2 at 1600 °C (UO_2 : $CaCO_3$: SiO_2 = 1 : 1 : 1).

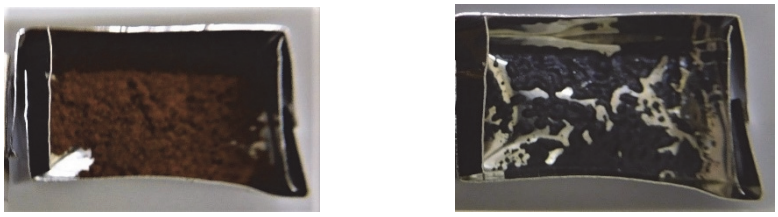

(a) Before heat treatment (b) After heat treatment

Figure 6. Optical images of the simulated MCCI debris (U-Ca-Si-O system) synthesized by heat treatment in 2% O_2 at 1600 °C.

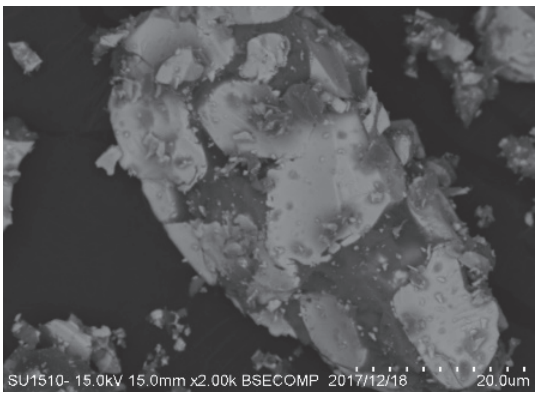

(a) SEM image by backscattered electron mode.

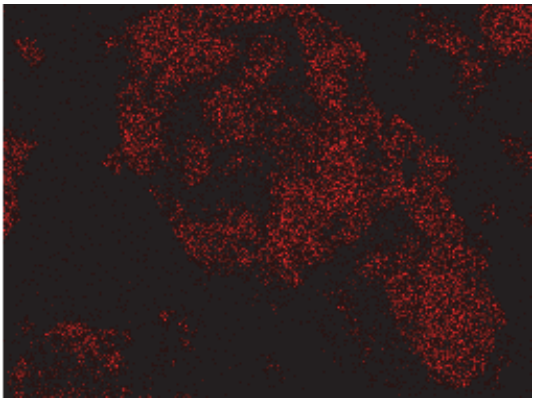

(b) U distribution mapping.

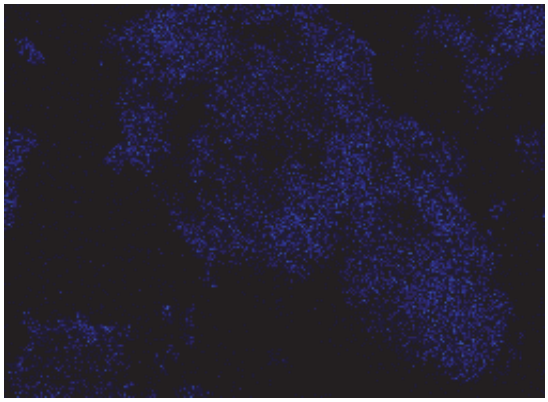

(c) Zr distribution mapping.

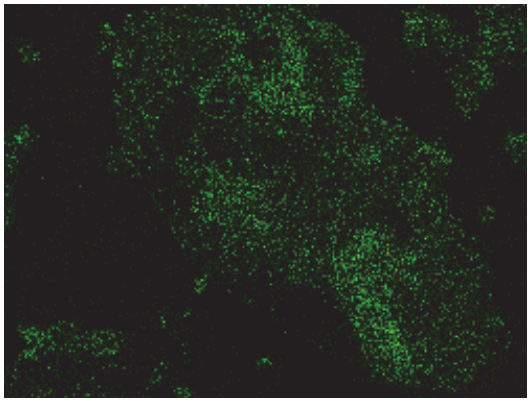

(d) Ca distribution mapping.

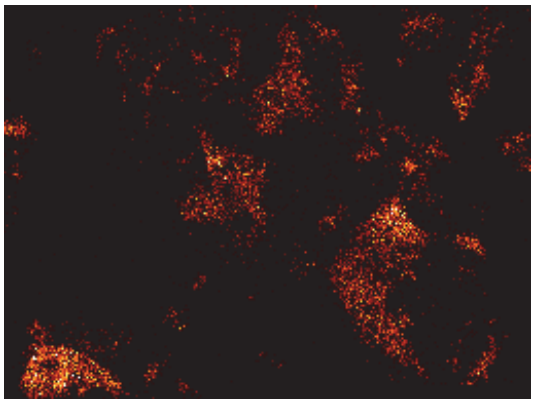

(e) Si distribution mapping.

Figure 7. SEM image and elemental mappings by EDX of the Zr-added MCCI debris (U-Zr-Ca-Si-O system) synthesized in 2% O_2 at 1600 °C (UO_2 : ZrO_2 : $CaCO_3$: SiO_2 = 1 : 1 : 1 : 1).

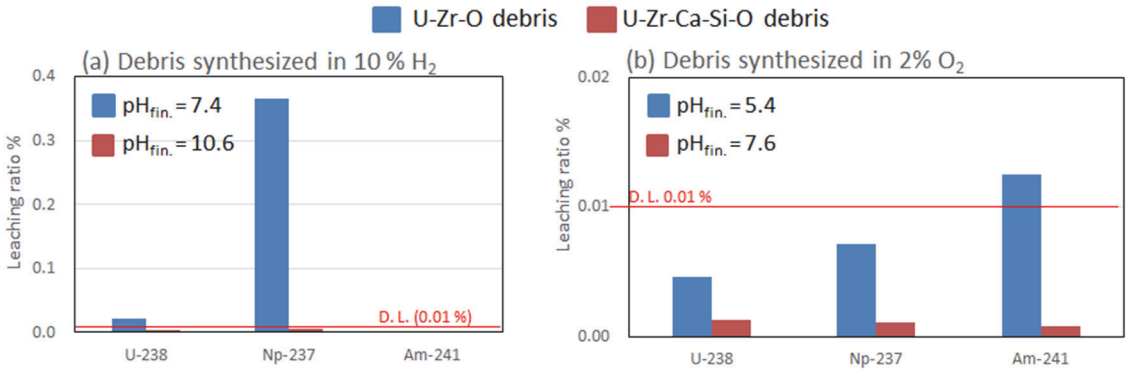

Figure 8. Comparison of the leaching ratios of the actinides from U-Zr-O debris and from Zr-added MCCI (U-Zr-Ca-Si-O) debris. (a): Debris synthesized in 10 % H_2 at 1600 °C, (b): Debris synthesized in 2% O_2 at 1600 °C,
Leaching test: for 31 days at 25 °C. "D. L." stands for "detection limit."

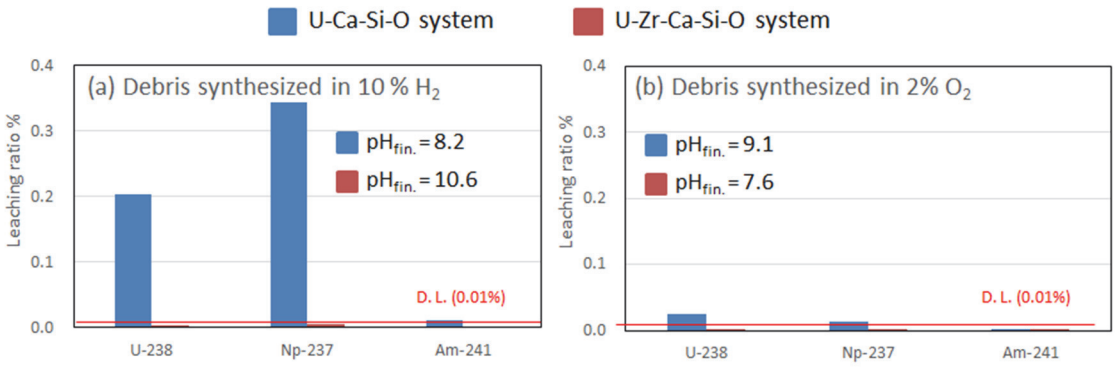

Figure 9. Comparison of the leaching ratios of the actinides from the MCCI (U-Ca-Si-O) debris and from the Zr-added MCCI (U-Zr-Ca-Si-O) debris. (a): Debris synthesized in 10% H_2 at 1600 ºC, (b): Debris synthesized in 2% O_2 at 1600 ºC,
Leaching test: for 31 days at 25 ºC. "D. L." stands for "detection limit."

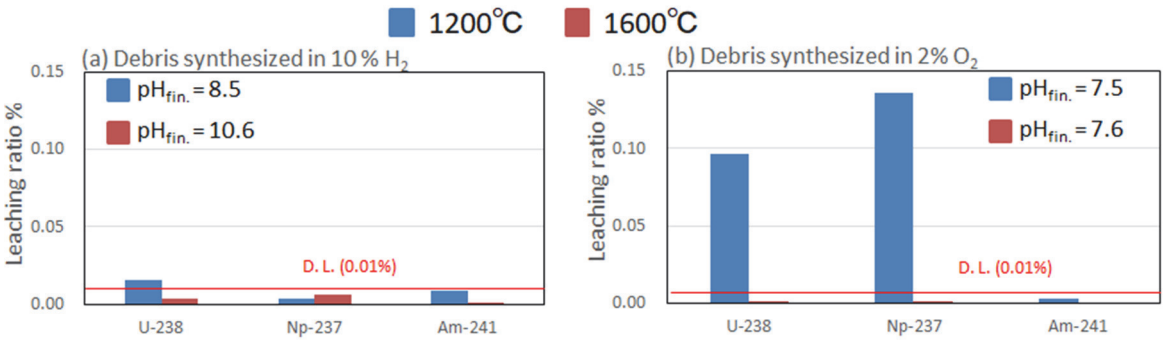

Figure 10. Comparison of the leaching ratios of the actinides from the Zr-added MCCI (U-Zr-Ca-Si-O) debris synthesized at 1200 and 1600 °C.
(a): Debris synthesized in 10% H_2, (b): Debris synthesized in 2% O_2,
Leaching test: for 31 days at 25 °C. “D. L.” stands for “detection limit.”

.

Supplementary materials

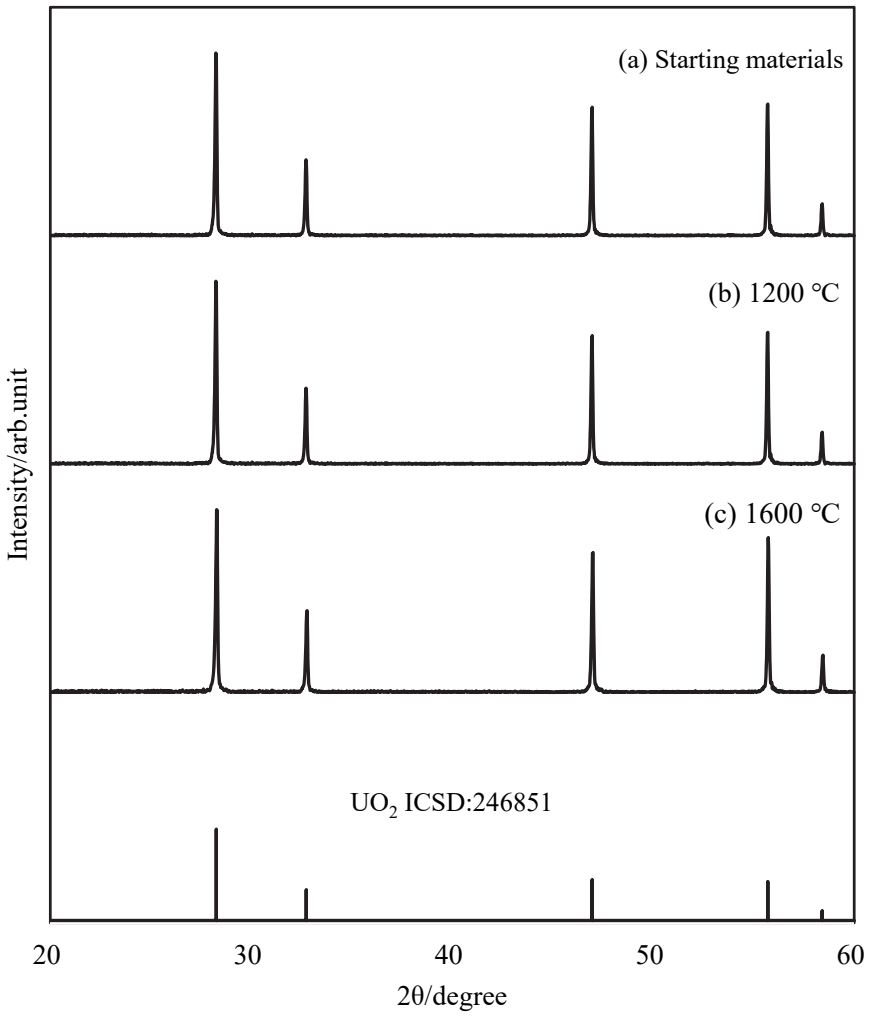

Figure S-1. XRD patterns of the simulated debris (U-O system) synthesized in 10% H_2 (UO_2).

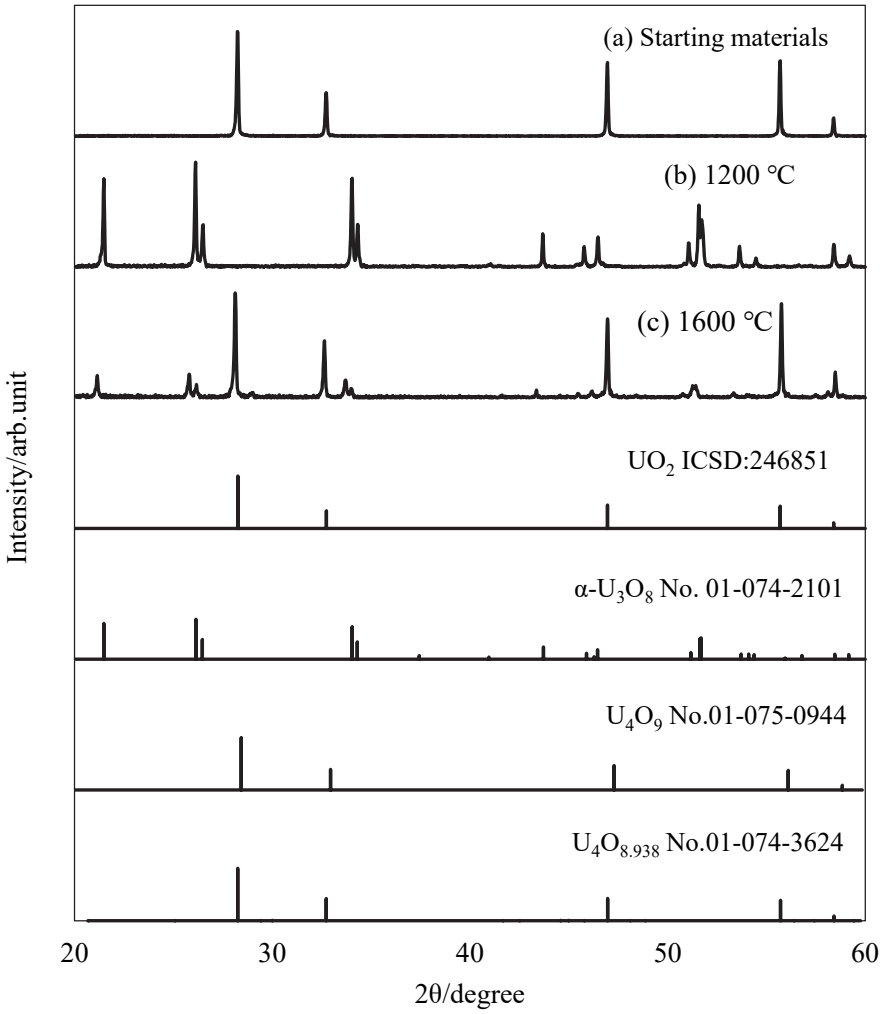

Figure S-2. XRD patterns of the simulated debris (U-O system) synthesized in 2% O_2 (UO_2).

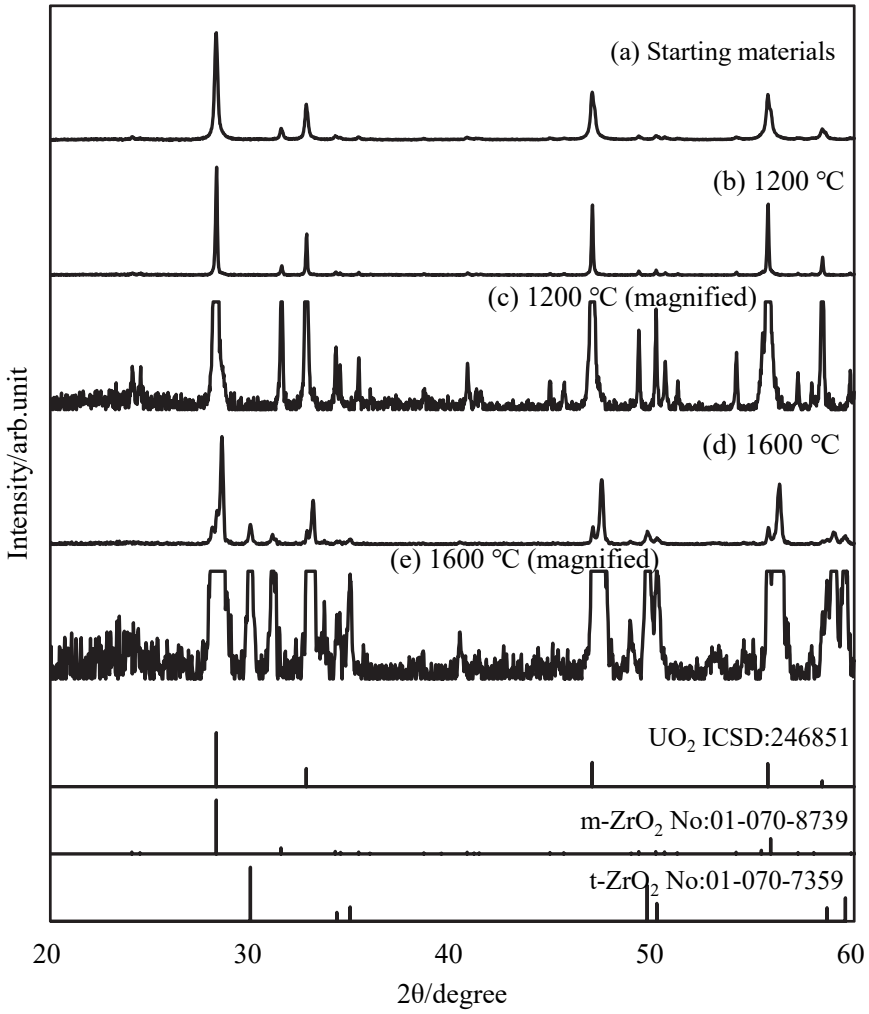

Figure S-3. XRD patterns of the simulated debris (U-Zr-O system) synthesized in 10% H_2 (UO_2 : ZrO_2 = 1 : 1).

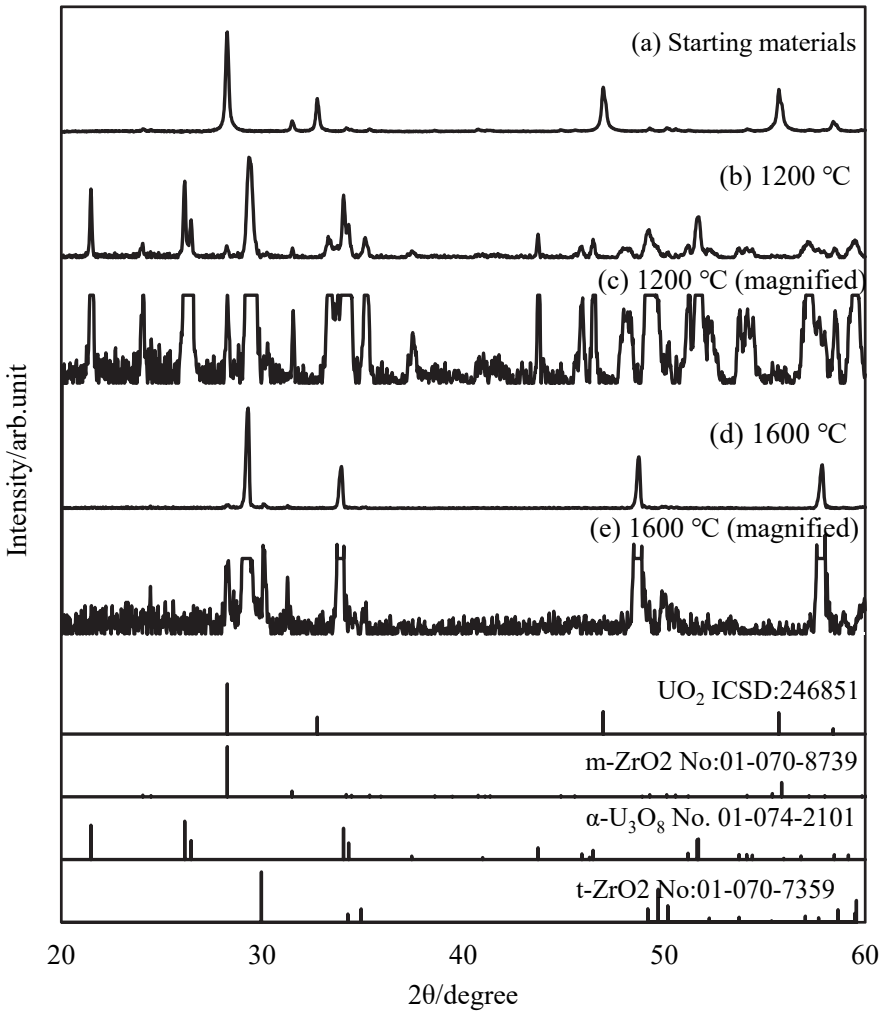

Figure S-4. XRD patterns of the simulated debris (U-Zr-O system) synthesized in 2% O_2 (UO_2 : ZrO_2 = 1 : 1).

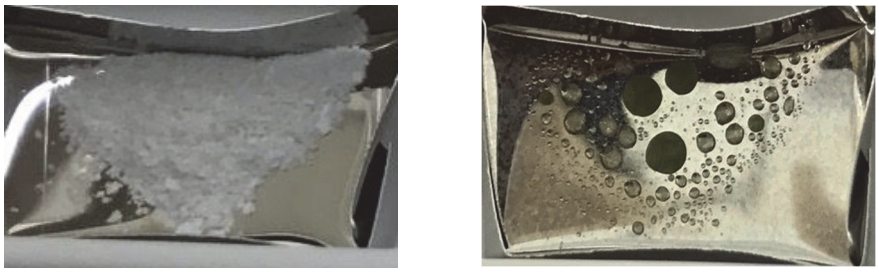

(a) (b)

Figure S-5. Optical images of the mixture of $CaCO_3$ and SiO_2 (1:1 in molecular ratio). (a) Initial material; (b) after heat treatment in 2% O_2 at 1600 °C.